A Regional Model of Shelf Circulation near Bass Strait: A New Upwelling Mechanism

SIMON R. EVANS AND JOHN F. MIDDLETON

School of Mathematics, University of New South Wales, Sydney, New South Wales, Australia

ABSTRACT

A study is made of the low-frequency, three-dimensional circulation and upwelling for the western region of Bass Strait, using oceanographic data and the Princeton Ocean Model. A novel radiation condition, which simulates the effect of an eastern shelf on Kelvin wave scattering, is successfully tested against analytic solutions for coastal-trapped wave (CTW) scattering and generation. Using a realistic bathymetry for the Bass Strait region, the model was forced with 8-day period zonal winds within the strait and a mode 1 CTW at the northwestern boundary. Results demonstrate the existence of a new mechanism for upwelling whereby at the cessation of westward winds within the strait, the residual poleward flow over the steeply sloping Tasmanian shelf separates from a gyre that develops over the more gently sloping topography near the mouth of the strait. The resultant divergence of the velocity field leads to large vertical velocities (34 m day^{-1}), and a plume of subthermocline water that is upwelled by 80 m and drawn 60 km toward the strait. While upwelling driven by the CTW paddle is less significant, data from the region suggest that the relative phase of the forcing mechanisms is such as to enhance upwelling over the shelf slope.

To examine the circulation and upwelling under realistic conditions, the model is forced by observed winds and the CTW paddle modulated using low-pass filtered sea-level data. The results reproduce some of the 30 cm s^{-1} and 20-cm variability apparent in current and sea level data obtained for the region. Moreover, the combined wind and CTW forcing is predicted to lead to upwelling rates of 34 m day^{-1} and the growth of an upwelled plume of subthermocline water that is displaced 120 m in the vertical and 80 km toward the strait.

1. Introduction

It is now recognized that large straits and bays can greatly influence the low-frequency circulation on adjoining shelves. Wright et al. (1987) and Webster and Narayanan (1988) identified the circulation in Hudson Strait as being important in driving the observed circulation on the Labrador shelf. Cahill et al. (1991) showed that the current variability on the west New Zealand shelf is driven by the circulation within Cook Strait. Freeland et al. (1986), and later Church and Freeland (1987), concluded that the coastal-trapped waves (CTWs) observed on the east Australian shelf were somehow driven by the circulation within Bass Strait (Fig. 1), and possibly by that farther to the west. Both modeling studies (Middleton 1991, 1994) and analyses of data (Baines et al. 1991; Middleton and Black 1994) have shown that local winds within the strait and CTWs incident from the western Bight region dominate the forcing of the 10–20-day band circulation within Bass Strait.

Little is known, however, about the three-dimensional shelf circulation adjacent to the mouths of large sea straits. While Middleton (1991) has shown that CTW scattering may lead to a shelf circulation dominated by the first three CTW modes, the solutions presented were for an idealized rectangular strait geometry and only barotropic long-wave modes were considered. The three-dimensional nature of the circulation adjacent to Bass Strait remains to be determined.

For the shelf west of Bass Strait, few data exist regarding currents or the hydrographic structure. Upwelling does seem to occur at the southwest corner of the strait. Observations near King Island (Fig. 1) show that bottom temperature can drop by 2°C over a day or two during the passage of intense storms (Blackman et al. 1987). Data presented by Gibbs et al. (1986) also show that some of the largest chlorophyll-*a* maxima occur in this region.

Our objective here is to investigate the nature of the circulation and upwelling for the western shelf region. To this end we adapt the Princeton Ocean Model (Blumberg and Mellor 1987) to a region encompassing the western strait, adjacent shelf and deep ocean. The model is to be forced by local winds and by a mode 1 CTW "paddle" off Portland (Fig. 1). The paddle is taken to represent energy that is the result of wind forcing on the shelves of western Victoria and South Australia. Other models of wind-forced circulation have been de-

Corresponding author address: Dr. John F. Middleton, School of Mathematics, University of New South Wales, Sydney 2052, Australia.
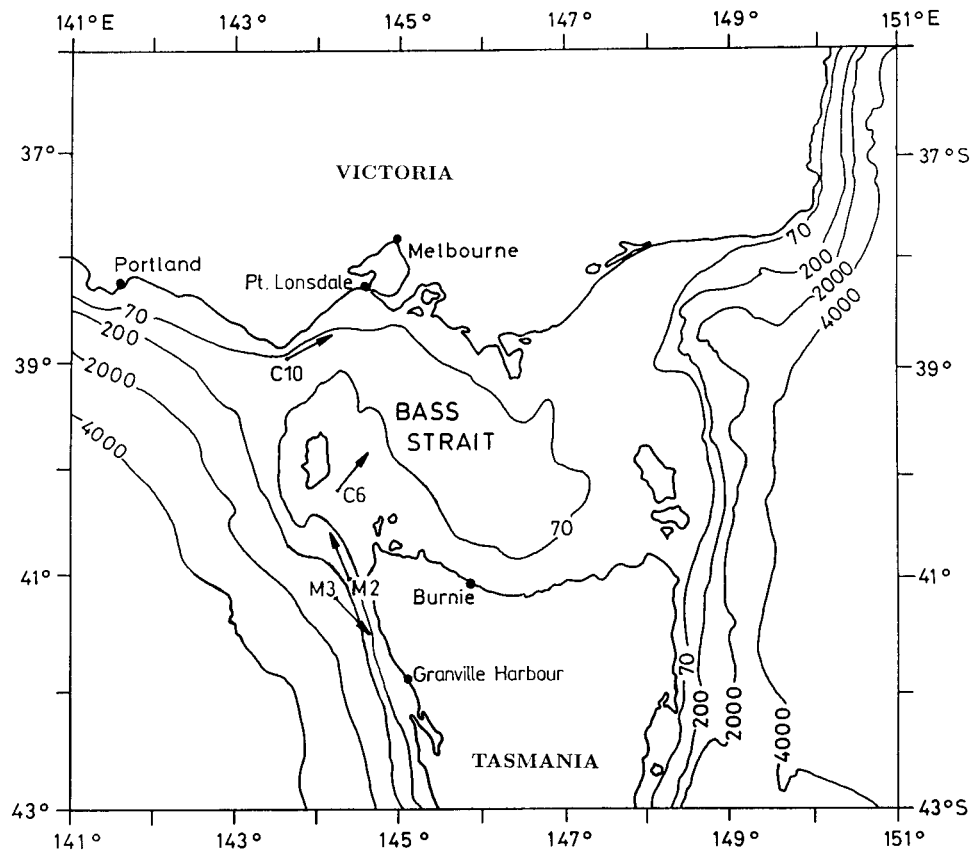E-mail: John.Middleton@unsw.edu.au

FIG. 1. The bathymetry of the Bass Strait region (isobath depths in meters). The current meter sites C6, C10, M2, and M3 are labeled. The directions of the major axes are indicated: for C10, the direction is for the 56-m depth record. Sea level data were obtained from Portland, Point Lonsdale, Burnie, and Granville Harbour.

veloped, though these have been barotropic (Middleton and Black 1994) or have adopted unrealistic open boundary conditions at the mouths of the strait (Fandry et al. 1985). One feature of the present model is that a novel radiation condition (Gardiner-Garden and Middleton 1996) is adopted to close the eastern strait mouth and properly allow for the partial reflection of Kelvin wave energy back into the strait (Middleton 1991).

An additional goal of the analysis is to validate the model and boundary conditions against analytic solutions for CTW wave scattering, as well as against observations of currents and sea level variability. To our knowledge, few published attempts have been made to validate primitive equation models of CTW or wind-forced shelf circulation. These include direct comparisons with analytic theories for CTW propagation (e.g., Wilkin and Chapman 1990; Slordal et al. 1994; Roed et al. 1995), as well as several quantitative comparisions with data (e.g., Werner et al. 1993; Davies and Jones 1992; Oey et al. 1995). The data to be used here were collected through a collaborative field program involving the C.S.I.R.O., the Victorian Institute of Marine Sciences, and the University of New South Wales. Unfortunately, several moorings were lost to trawlers so that

CTD coverage of the western shelf is poor. Nonetheless, using the remaining data we will validate some important predictions of the model and provide evidence that the scattered CTWs near Bass Strait lead to significant upwelling.

In section 2, the model and boundary conditions are outlined. Model solutions for an idealized rectangular strait geometry are obtained and compared with analytic results in order to evaluate the validity of the boundary conditions. In section 3, the model is adapted to a realistic bathymetry, and the circulation and upwelling that results from the CTW paddle and local winds is established. A review of the relevant observations for the region is given in section 4, and simulations of the low-frequency circulation are compared with data from the region.

2. Model description and preliminary verification

The Princeton Ocean Model is a three-dimensional, primitive equation, free surface model (Blumberg and Mellor 1987). Using the hydrostatic and Boussinesq approximations, the momentum equations are

$$\frac{\partial \mathbf{u}}{\partial t} + \mathbf{u} \cdot \nabla_h \mathbf{u} + w \frac{\partial \mathbf{u}}{\partial z} + \mathbf{k} \times f \mathbf{u}$$

$$= -\frac{1}{\rho_0} \nabla_h p + \frac{\partial}{\partial z}\left(K_M \frac{\partial \mathbf{u}}{\partial z}\right) + \mathbf{F} \qquad (2.1a)$$

$$0 = -\frac{1}{\rho} \frac{\partial p}{\partial z} - g, \qquad (2.1b)$$

where $\mathbf{u} = (u, v)$ is the horizontal velocity, w is the vertical velocity, ∇_h is the horizontal vector operator ($\partial/\partial x, \partial/\partial y$); ρ and ρ_0 are in situ and reference densities, p is pressure, $f = -9.13 \times 10^{-5} \text{ s}^{-1}$ is the Coriolis parameter, and K_M is the vertical eddy diffusivity of momentum. Horizontal diffusion terms are contained in $\mathbf{F} = (F_x, F_y)$, which depends on an eddy diffusivity for momentum A_M (Blumberg and Mellor 1987). The remaining equations are the continuity equation, $\nabla_h \cdot \mathbf{u} + \partial w/\partial z = 0$, and the conservation equations for potential temperature θ and salinity S,

$$\frac{\partial(\theta, S)}{\partial t} + \mathbf{u} \cdot \nabla_h(\theta, S) + w\frac{\partial(\theta, S)}{\partial z}$$

$$= \frac{\partial}{\partial z}\left(K_H \frac{\partial(\theta, S)}{\partial z}\right) + F_{(\theta, S)}, \qquad (2.1c)$$

where K_H is a vertical diffusivity for heat and salinity, and F_θ, F_S are horizontal diffusion terms, which include a diffusivity for heat and salinity A_H. Density is computed by a nonlinear equation of state $\rho = \rho(\theta, S, p)$.

To solve the above, Eqs. (2.1) are transformed to a stretched vertical σ coordinate and approximated using an Arakawa C grid. Using a vertically integrated version of (2.1a), depth-averaged velocities $(\bar{u}, \bar{v})$ and elevation η are computed using an explicit step over an "external" time interval Δt_{ext}. After many such steps, these values are used to update (2.1) over a longer "internal" time step Δt_{int}.

In order to test the boundary conditions, the model was configured for a rectangular idealized strait (Fig. 2) so that results could be compared with existing analytic solutions for the circulation forced by both incident CTWs and local winds. The shelf bathymetry was taken from Portland and assumed uniform in the alongshelf direction. The depth, width, and length of the strait were taken to be $h_0 = 60$ m, $W = 198$ km, and $L = 404$ km respectively. A rectangular grid was used with Δx ranging from around 2 km over the shelf break to 25 km offshore and Δy ranging from 12 km to 20 km (see Fig. 2a). The values of Δx were chosen in part to minimize spurious cross-isobath pressure gradients associated with the σ-coordinate representation (Mellor et al. 1994). For this configuration 20 σ levels were used, distributed logarithmically near the surface and uniformly throughout the rest of the water column. The time steps were chosen to be $\Delta t_{\text{ext}} = 8$ s and $\Delta t_{\text{int}} = 279$ s. The initial temperature and salinity profiles (Fig. 3) were computed using data collected from the western Bass Strait region during au-
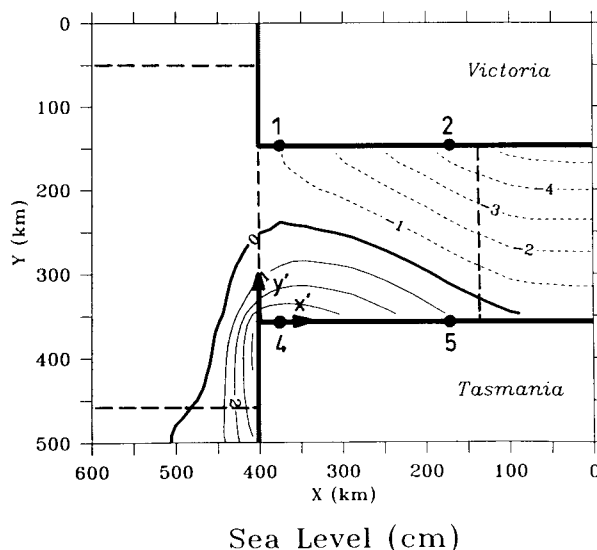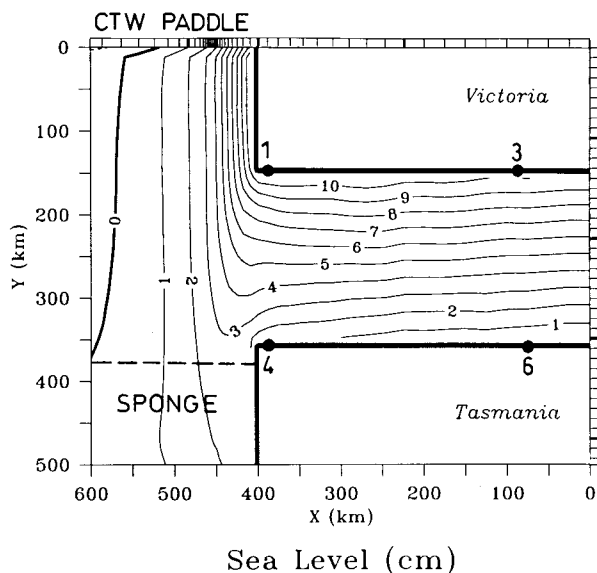

Sea Level (cm)

Sea Level (cm)

FIG. 2. (a: top) Sea level results (in cm) at day 2 obtained using a rectangular strait bathymetry, for an 8-day period mode 1 CTW paddle (coastal amplitude 11.5 cm). The sites of data extraction within the strait are numbered. The large dashed line indicates the northern limit of the sponge. (b: bottom) As for (a) but for wind-forcing by an 8-day period zonal wind stress with amplitude 0.1 Pa. The large dash lines indicate the edges of the wind tapers: the inner edges are at $x = 400$ km and $x = 140$ km. In both cases the strait depth is 60 m, the 1000-m shelf isobath coincides with $x = 500$ km, and the model domain extends to $x = 760$ km. The temporary (x', y') coordinate system for the analytic models (2.3) and (2.6) is shown.

tumn 1991. The diffusivities were chosen to be $K_M = 9 \times 10^{-4} \text{ m}^2 \text{ s}^{-1}$, $K_H = 2 \times 10^{-4} \text{ m}^2 \text{ s}^{-1}$, and $A_H = A_M = 50 \text{ m}^2 \text{ s}^{-1}$. Surface fluxes of θ and S were set to zero. In the validation study below, bottom stress was set to
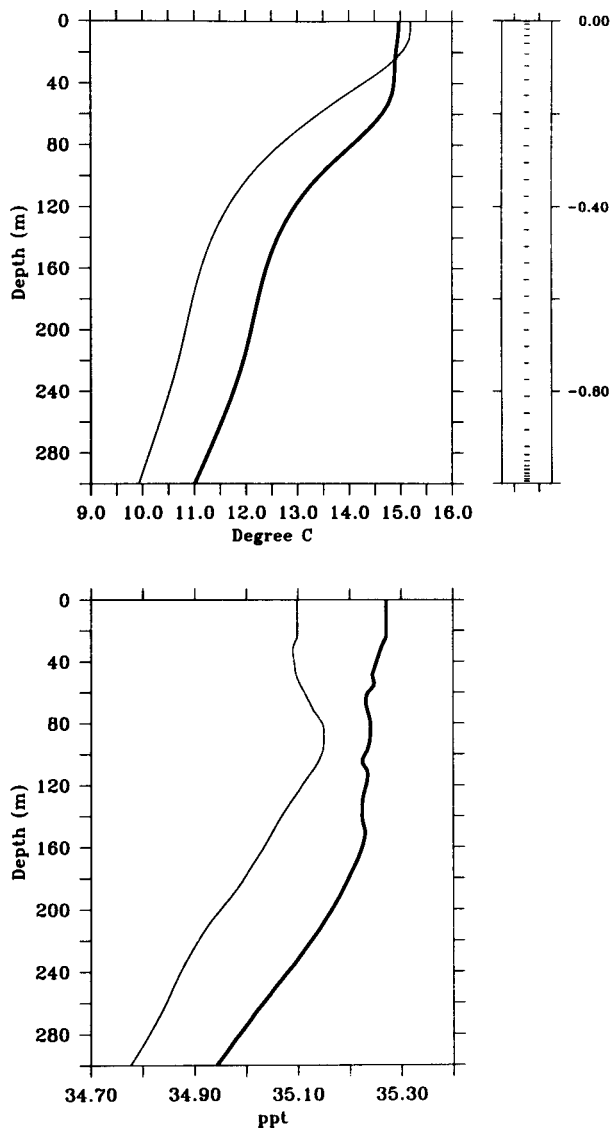
FIG. 3. The initial (a: top) temperature and (b: bottom) salinity used in the model. Light lines show summer values; bold lines show autumn values. The curves were computed using data collected off the northwest shelf of Tasmania on 9 January 1991 and 14 May 1991. The plot at top right shows the 40 σ-coordinate levels used in the model. The spacing obeys power-law distributions near the surface ($\sigma = 0.0$) and bottom ($\sigma = -1.0$), with constant spacing in the interior.

zero so that a comparison might be made with inviscid analytical results.

At the western (deep ocean) boundary, zero-gradient conditions $\eta_x = \overline{u}_x = \overline{v}_x = 0$ were applied while conditions for u, v, θ, S were determined by applying an implicit Orlanski radiation condition to the residuals $u' = u - \overline{u}$, $v' = v - \overline{v}$, etc. (e.g., Chapman 1985). The horizontal gradients of the CTW eigenfunctions are small at this boundary and should be well approximated by the zero-gradient condition for η, $\overline{u}$, $\overline{v}$. The radiation condition for the depth-dependent residuals allows in-

ternal waves to propagate out of the model domain. At the southern open boundary, an implicit Orlanski radiation condition was applied to all variables. Near the boundary, a Rayleigh sponge condition was applied to η, $\mathbf{u}$, $\overline{\mathbf{u}}$ and Newtonian cooling to perturbations in θ and S to absorb incoming energy and momentum (e.g., McCreary et al. 1991). Using a power law ($y^{-1.6}$), the damping timescale was decreased from 40 days at $y = 372$ km to 5.5 h at the boundary $y = 516$ km.

In the case of periodic CTW forcing alone, the boundary condition at $y = 0$ (see Fig. 2a) was specified using a mode 1 inviscid CTW eigenfunction, calculated using the Brink and Chapman (1985) programs and the local bathymetry and density field. For example, with $F_n(x, z)$ the nth eigenfunction for CTW pressure, the boundary solution for η is

$$\eta = a_I F_1(x, 0) \, \sin(\omega t)/\rho g, \qquad (2.2)$$

where the period of the forcing was chosen to be 8 days (typical for the Bass Strait region) and a_I denotes an amplitude. To allow the CTW to propagate smoothly into the (viscous) domain, the viscosities A_H and A_M were ramped linearly over 60 km from zero at the boundary to their interior values. In the case of wind forcing alone, the CTW paddle was set to zero. A requirement for the eastern strait boundary is that it behave naturally with respect to the transmission and reflection of low-frequency energy. Because of limitations on computing resources, modeling the eastern shelf and ocean was not practical and following Gardiner-Garden and Middleton (1996), we outline a new numerical radiation condition that simulates the presence of an eastern ocean.

a. Solutions for scattering and an eastern strait boundary condition

Consider first the circulation within the strait, which is driven by the scattering of a CTW incident on the western mouth. A CTW that enters the rectangular domain shown in Fig. 2 will act to raise/lower sea level at the northwest corner of the strait and drive a Kelvin wave along the "Victorian" coast (Middleton 1991). This wave will in turn scatter energy into CTWs on the eastern shelf and also drive a reflected Kelvin wave, which propagates to the west along the "Tasmanian" coast. The reflected wave arises from the fact that since CTWs can only propagate with the coast on the left (Southern Hemisphere), sea level variations must vanish at the southeast corner of the strait. [Data from the region (Freeland et al. 1986) suggest there to be little CTW generation on the east Tasmanian coast, which could otherwise affect sea level variability at the southeast corner.] These ideas are illustrated in Fig. 2a where the (model) sea-level field is presented at a time of maximum forcing by the incident CTW paddle. The reflected Kelvin wave acts to keep sea level variations small along the Tasmanian coast, whereas at the western strait

mouth, the intensified sea level gradients drive an across-isobath velocity, which in turn generates a scattered CTW field on the western shelf.

To develop the strait boundary condition, consider the barotropic solution for low frequency ($\epsilon = \omega/|f| \ll 1$) sea level variations within the strait (Middleton 1991), which can be written as

$$e^{i\omega t}\eta(x', y', t)$$
$$= Te^{\alpha y' + il_0 x'} + Re^{-\alpha y' - il_0 x'}$$
$$+ \sum_{n=1}^{\infty} (d_n^e e^{r_n(x'-L)} + d_n^w e^{-r_n x'}) \sin(r_n y' + \epsilon), \quad (2.3)$$

where a temporary coordinate system (x', y') is assumed (Fig. 2). The first two terms on the right-hand side represent a pair of Kelvin waves with amplitudes T and R, decay scale $\alpha^{-1} = \sqrt{gh_0}/|f|$ and wavenumber $l_0 = \omega/\sqrt{gh_0}$. The transmitted wave (amplitude T) propagates eastward along $y' = W$ (since $f < 0$), and the reflected wave (amplitude R) propagates westward along $y' = 0$. The last term is a set of evanescent Poincaré wave modes that are generated at the eastern and western ends of the strait with amplitudes d_n^e and d_n^w, respectively, and decay into the strait with a scale $1/r_n = W/n\pi$, where W is the strait width.

A boundary condition for the eastern strait mouth can be found by noting that the Poincaré wave contribution to coastal sea level from (2.3) is of order $\epsilon = \omega/|f|$, which is small for the 10–20-day variability that characterizes the region. We therefore assume that only Kelvin waves make a significant contribution to coastal sea level, and since sea level variations vanish at the southeast corner of the strait, $R = -T$, and the sea level variations satisfy

$$\eta(L, y', t) = 2T \sinh(\alpha y')e^{-i\omega t} \quad (2.4)$$

at the eastern mouth. We assume here (and find) that the solution at the eastern boundary will consist only of Kelvin waves. Poincaré waves generated at the western strait mouth should not influence sea level at the eastern end since their decay scale of $W/\pi \approx 63$ km is small compared to the 400-km length of the strait. The use of (2.4) should also preclude the generation of Poincaré waves at the eastern mouth.

To implement the boundary condition (2.4), the amplitude of the transmitted Kelvin wave $T \exp(-i\omega t)$ must be diagnosed. To further ensure that Poincaré waves do not contaminate the estimate of T, we follow Gill (1982) by introducing the variable $q = \eta - \overline{u} \sqrt{h_0/g}$ and define

$$Q = \frac{1}{2}[q(y' = 0) + q(y' = W)], \quad (2.5)$$

which will filter out any odd Poincaré wave contribution to the estimate of T. With η given by (2.4) and $\overline{u}$ geostrophic, the amplitude T is specified by $T = -Q(1 + e^{-\alpha d})^{-1}$. The value of Q is determined from the field variables η and $\overline{u}$ within the model. The boundary con-

dition (2.4) was applied to η and, through geostrophy, to $\overline{u}$. Lastly, $\overline{v}$ was set to zero. The boundary condition (2.4) only applies to depth-independent, inviscid motion, and to minimize the development of a frictional boundary layer the frictional parameters A_H and A_M were tapered linearly to zero near the eastern strait boundary over a range of about 70 km. In addition, we assume (and find) that internal wave motion is small at this end of the strait using the reflective boundary conditions $u = \overline{u}$ and $v = \overline{v}$ for the depth-dependent velocities (the values of temperature and salinity are simply fixed to be equal to their initial values).

b. Validation

Model results were obtained using the mode 1 CTW paddle described above with a value of a_1 corresponding to a sea level amplitude of 11.5 cm at the coast. The model was run for 12 days from a state of rest. Solutions for sea level at day 2 (Fig. 2a) are in qualitative agreement with those obtained analytically by Middleton (1991), and with those from a barotropic model that includes an eastern shelf (Middleton and Black 1994). A small kink in sea level evident near the paddle is associated with the adjustment of the inviscid wave into the viscous interior. As required, sea level variations are small along the Tasmanian coast.

A quantitative comparison with the analytic model (2.3) was made by extracting time series of coastal sea level from the model for the last 8 days of forcing. The first 2 days were discarded in order to avoid any distortion by initial transients. The model time series were then Fourier decomposed into a mean μ, amplitude a, and phase δ at coastal sites 1, 3, 4, and 6 within the strait (Fig. 2), whereby $\eta = \mu + a \sin(\omega t - \delta)$. Results were also obtained from the analytic model (2.3) by assuming an 11.5-cm incident sea-level perturbation and by neglecting the small Poincaré wave contribution to coastal sea level ($\epsilon \approx 0.1$ for $2\pi/\omega = 8$ days). As shown in Table 1, the agreement between the numerical and analytical results is good. The amplitudes at sites 3, 4, and 6 around the strait are nearly identical, and the phase lags agree to within 1.3 h or 0.7% of the 8-day period. The means from the numerical model are small. A similar analysis, made by forcing the model over 28 days, shows that stable, consistent solutions are obtained with the boundary conditions adopted.

The second model validation case involves the circulation that arises from oscillatory zonal wind forcing over the strait, where $\tau^x = \tau_0 \sin(\omega t)$, $\tau^y = 0$, $2\pi/\omega = 8$ days, and $\tau_0 = 0.1$ Pa. The eastern strait boundary condition is essentially a depth-independent condition based upon the scattering of *free* Kelvin waves. This being the case, we cannot allow the wind field to create forced waves at the eastern boundary. Hence the wind field was tapered from its interior value at $x = 140$ km to zero near the eastern boundary, $x \leq 40$ km (Fig. 2). The winds were also tapered to zero near the other open

TABLE 1. Comparison of numerical and analytic results for sea level variability at various sites around the rectangular strait used in the validation studies. The analytic results for the wind-driven case were obtained using an effective strait length of 295 km. Since the phase calculation can give unreliable results for small amplitudes, some phases have been omitted.

Case	Site	μ (cm)		α_I (cm)		Phase (h)	
		Model	Analytic	Model	Analytic	Model	Analytic
CTW	1	0.7	0.0	11.5	11.5	0.0	0.0
	3	0.6	0.0	11.6	11.4	4.5	5.8
	4	0.2	0.0	1.6	2.0	—	—
	6	0.1	0.0	0.4	0.4	—	—
Wind	1	0.1	0.0	0.6	0.3	—	—
	2	0.2	0.0	4.2	3.8	2.1	1.1
	4	0.4	0.0	−4.3	−4.6	9.5	−3.0
	5	0.2	0.0	−1.1	−1.1	9.0	−9.2

boundaries (also shown in Fig. 2), so that the boundary conditions adopted for CTW forcing could be used there.

Analytic solutions for wind forcing over a rectangular strait have been given by Middleton and Viera (1991) and Hannah (1992). The Kelvin wave response has been shown to be of the form

$$\eta = K \frac{\tau_0 L e^{-i\omega t}}{\rho_0 g h_0} \left[\frac{x'}{L} - \left(1 - \frac{y'}{W} \right) \right], \qquad (2.6)$$

where L and W denote the length and width of the strait and K is a nondimensional function of the strait geometry. This solution represents a superposition of two forced Kelvin waves, and the result is a plane of sea level that oscillates about an axis joining the northwest and southeast corners of the strait. The numerical solutions obtained reproduce this oscillating plane of sea level in the interior of the strait quite well (Fig. 2b), although near the western mouth of the strait, the pattern is modified by the Poincaré waves generated by the inclusion of the adjacent shelf. At the eastern end of the strait, the sea level contours become more parallel with the strait axis due to the tapering of the wind stress and imposition of the strait boundary condition (2.4).

To further evaluate the numerical results, time series of sea level for days 4–12 were extracted from the model at sites 1, 2, 4, and 5 shown in Fig. 2b. Since the numerical and analytic model results use a different fetch of wind forcing, a comparison between the two was made by varying the length of the strait in the analytic model. The best fit of the amplitudes and phases was found by assuming the length of the strait to be 295 km for the analytic model, that is, the model circulation driven by the tapered winds shown in Fig. 2b is equivalent to the (analytic) circulation driven by a spatially constant wind with a fetch of 295 km. This length is approximately equal to that of the untapered region of forcing of the numerical model.

The results for the mean, amplitude, and phase obtained from the numerical and analytical models are again shown in Table 1, although the discrepancies are larger than found for the case of forcing by an incident CTW. At sites 2 and 4, where the response is largest,

the numerical and analytic amplitudes differ by as much as 10%. The phase lags at site 4 also differ by 12 h or 6.25% of the 8-day forcing period. At sites 1 and 5, where the response is smaller, the amplitudes are in somewhat better agreement. In conclusion, while the general agreement found suggests that the boundary conditions adopted are appropriate, the quantitative differences show the variation that can be expected through the use of the wind tapers.

3. Realistic bathymetry: Idealized forcing

Here we discuss aspects of the circulation at the western end of Bass Strait, forced by a zonal periodic wind stress or an incident periodic CTW. The CTW paddle, imposed at the northwest open boundary, is meant to represent the wind-forced circulation generated along the western Victorian and South Australian coasts, which lie outside of the model domain. The model will also be forced by a zonal component of wind within the strait. Alongshelf winds between the paddle and the strait are neglected, although estimates suggest this would only add a further 2–3 cm s^{-1} to the total circulation. The aim is to gauge the relative importance of local winds and incident CTWs with regard to the circulation and upwelling on the adjacent shelf.

The assumed bathymetry is shown in Fig. 4a. The isobaths off western Victoria and Tasmania were straightened in order to allow CTWs to enter and leave the model domain smoothly. Bass Strait itself was given a rectangular, flat-bottomed extension at its eastern end so that the circulation there can adjust to Kelvin waves, which can then be appropriately diagnosed by the eastern strait boundary condition. The extension is of a length comparable to the gravest evanescent Poincaré mode that might be generated at the western end, so that the eastern boundary remains uncontaminated.

The rectangular horizontal grid chosen is shown at the edges of Fig. 4a, with Δx ranging from less than 2 km over the shelf break to 25 km offshore and Δy ranging from 12 km to 20 km. To resolve both the surface and bottom boundary layers, 40 σ-levels were used in the vertical with power-law spacings near the surface
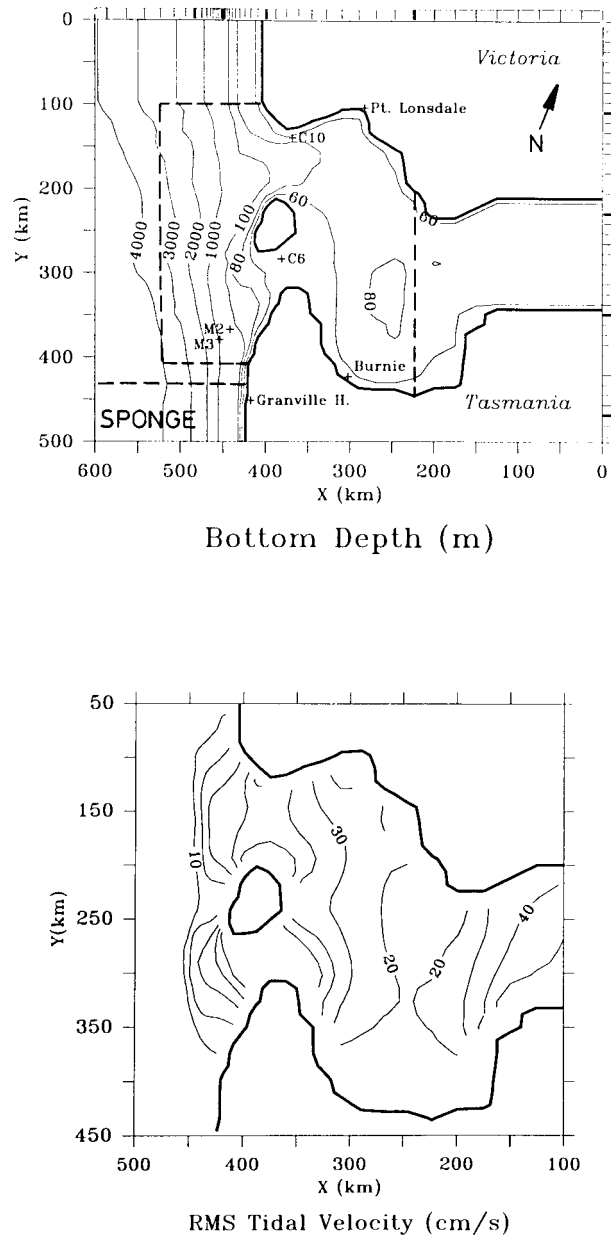
Bottom Depth (m)

RMS Tidal Velocity (cm/s)

FIG. 4. (a: top) The semirealistic bathymetry of Bass Strait. Isobath depths are in meters. Current meter sites and grid resolution are indicated, and the large-dash lines indicate the inner edges of the wind tapers. The model domain extends to $x = 760$ km and $y = 650$ km. (b: bottom) The rms M_2 tidal velocity (units cm s^{-1}), computed using a barotropic version of the model.

and bottom. The σ-coordinate spacings are shown in Fig. 3. The Mellor-Yamada level 2.5 closure scheme was used to predict K_M and K_H.

For the Bass Strait region, the dominant M_2 tidal currents can exceed 0.5 m s^{-1} (Fandry et al. 1985), and will be important both for vertical mixing and for bottom stress. Here, the effects of the tides were incorporated into the model through the drag law for bottom stress, $\boldsymbol{\tau}_b = \rho_0 C_D \mathbf{u}(|\mathbf{u}|^2 + \sigma_{M_2}^2)^{1/2}$, where $C_D = 2.0 \times 10^{-3}$ is

a drag coefficient and σ_{M_2} is the rms speed of the M_2 tidal current (e.g., Wright and Thompson 1983). The tidal velocities were calculated using a barotropic implementation of the model, forced at the open boundaries by the M_2 tidal amplitudes given by Fandry et al. (1985). The resultant rms tidal velocities shown in Fig. 4b compare well with similar results obtained from a larger domain model (Black 1992). Since the drag law may be only approximate for stratified sloping shelves, a more complicated parameterization of bottom stress did not seem warranted, and only the dominant M_2 component was used.

To allow the mode 1 CTW to adjust smoothly into the domain, the drag coefficient C_D was set to zero over the first 36 km near the paddle boundary $y = 0$ and then ramped to its interior value over a further 36 km. The horizontal diffusivities, A_H and A_M, were ramped from around 7 m^2 s^{-1} at $y = 0$ to the constant interior value of 50 m^2 s^{-1} over 84 km. These values were also used for the wind-forced solutions since the model is to be forced with both CTWs and observed winds in the following section. In the wind-forced case below, the northern boundary condition is simply prescribed as a paddle of zero amplitude. To typify some of the larger events in the data, we fix the coastal amplitude of the mode 1 CTW paddle to be 20 cm and the period to be 8 days. For the winds, only a through-strait (zonal) component is chosen for which $\tau^x = \tau_0 \sin(\omega t)$, $2\pi/\omega = 8$ days, and $\tau_0 = -0.2$ Pa. The wind stress tapers are shown in Fig. 4a.

We consider first the wind-forced case in which the model was started from rest and run for 12 days. The eastward stress at day 10 lowers sea level by 4–5 cm on the Tasmanian coast, leading to a jet of 30–40 cm s^{-1} on the western shelf and also between King Island and Tasmania (Fig. 5a). Cross-sectional plots of the western shelf jet at $y = 400$ km are presented in Fig. 6a. At day 10, the currents are approximately to the north at depths less than 200 m. Associated with these currents are vertical velocities that exceed 0.4 mm s^{-1} (34 m day^{-1}) over the shelf slope (Fig. 6b), and the 12°C isotherm has been raised by 90 m from an initial depth of 210 m (Fig. 6c). As shown in Fig. 7a, the upwelled water is then advected some 60 km toward the strait as a plume 10 km wide. The 12.5° isotherm is raised from an initial depth of 160 m to 73 m.

Before attempting an explanation of the upwelling mechanism, we will examine the importance of Ekman upwelling in the bottom boundary layer. The model was rerun with no bottom drag (no bottom boundary layer) and with the magnitude of the wind stress reduced ($\tau_0 = -0.15$ Pa) so that the velocity field might be similar in strength to that discussed above. The results (Figs. 6d–f) were quantitatively very similar to those obtained with bottom drag. That is, advection by the interior flow dominates the upwelling at depths greater than 120 m or so. Boundary layer upwelling is of some importance at lesser depths where the alongshore flow is larger. As
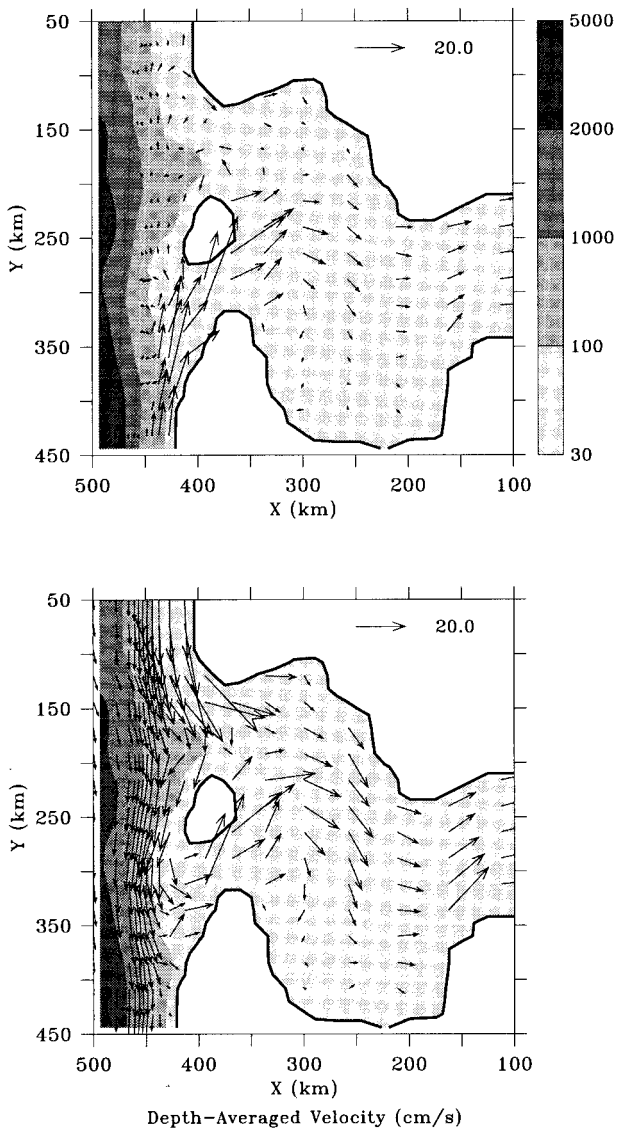
FIG. 5. (a: top) Depth-averaged velocity at day 10, as forced by an idealized 8-day period, 0.2-Pa wind stress. At this time the stress is in the negative x direction. The shading shows bathymetry in meters, indicated by the key. (b: bottom) Depth-averaged velocity at day 11 as forced by an 8-day period, 20-cm amplitude mode 1 CTW paddle. At the time shown, the paddle sea level is positive. Shading as in (a).

shown in Fig. 7b, the exclusion of bottom drag results in a smaller, deeper plume of upwelled water.

What is the cause of the deep upwelling, which occurs even in the absence of bottom drag? To illustrate, we will concentrate on days 6–10 of the simulation.

At day 6, when the wind is strongly westward, water is driven out of the strait mouth and turned southward in the direction of CTW energy propagation, producing the coastally trapped flow evident in Figs. 8a–c. The deep flow (e.g., Fig. 8b) is further focused by the narrow shelf south of $y = 400$ km, leading to downwelling at depths less than 200 m or so (Fig. 9a).

The "deep upwelling" phase of the process takes place following day 6 as the westward wind stress relaxes to zero at day 8. In adjusting to the diminishing wind stress, the current tends to follow isobaths and also be deflected to the left by the Coriolis force. Adjacent to the strait mouth, where the topographic slope is relatively gentle, the Coriolis effect dominates, resulting in the gyre shown in Fig. 8d. At a depth of around 100 m the currents are correspondingly reversed in the region north of $y = 400$ km. Farther south, the narrow shelf acts to restrict any deflection, and the flow remains poleward as before. The result is a strong horizontal divergence in the flow field at 100-m depth near the $y = 400$ km section (Fig. 8e), which in part leads to the upwelling at depths greater than about 100 m (Fig. 9b). This deep upwelling is further enhanced by the divergence of the flow at 200-m depth, which is also directed toward the strait (Fig. 8f), rather than poleward as at 100 m. This vertical shear is the result of the thermal wind associated with the downwelled isotherms at depths of 80–140 m (Fig. 9b).

After day 8 the process enters an "advection" phase. During this period the wind strengthens in an easterly direction. Water is drawn back into the strait (Figs. 8g–i) and the flow adjacent to the Tasmanian coast is now upwelling favorable (Fig. 9c). This phase continues until day 12 when the wind stress is again zero.

To examine the fate of the upwelled water, the model was run for a further 6 days. By day 15, the 12.5° isotherm was found to be downwelled to a depth of 250 m off the northwest coast of Tasmania; a net vertical displacement of 170 m over the 8 days of forcing. By day 18, the wind direction and currents on the shelf reverse, and the upwelling pattern is again established.

The importance of the nonlinear terms $\mathbf{u} \cdot \nabla \mathbf{u}$ for the upwelling process was also investigated by setting these terms to zero in the model. Terms involving the advection of temperature and salinity were retained. The results so obtained for w and temperature at day 10 (Figs. 6h,i) are very similar to those obtained with the nonlinear terms included (Figs. 6b,c), indicating that the deep upwelling is essentially a linear process.

Quantitative differences do exist, as shown by the results for the alongslope velocity (Figs. 6a and 6g). Time-averaged results also show that off the northern Tasmanian shelf at depths less that 100 m, the nonlinear terms produce a rectified flow of several centimeters per second directed toward the strait. While this flow does enhance the upwelling somewhat during the advection phase, the upwelled plume obtained without the nonlinear terms is similar to that shown in Fig. 7b. We conclude therefore that while the nonlinear terms and bottom friction are of some importance, the upwelling process is essentially linear in nature.

An overview of the circulation driven by the CTW paddle alone (no wind forcing) is shown in Fig. 5b. Since this mode 1 wave takes about a day to propagate to the upwelling region, results are presented at day 11
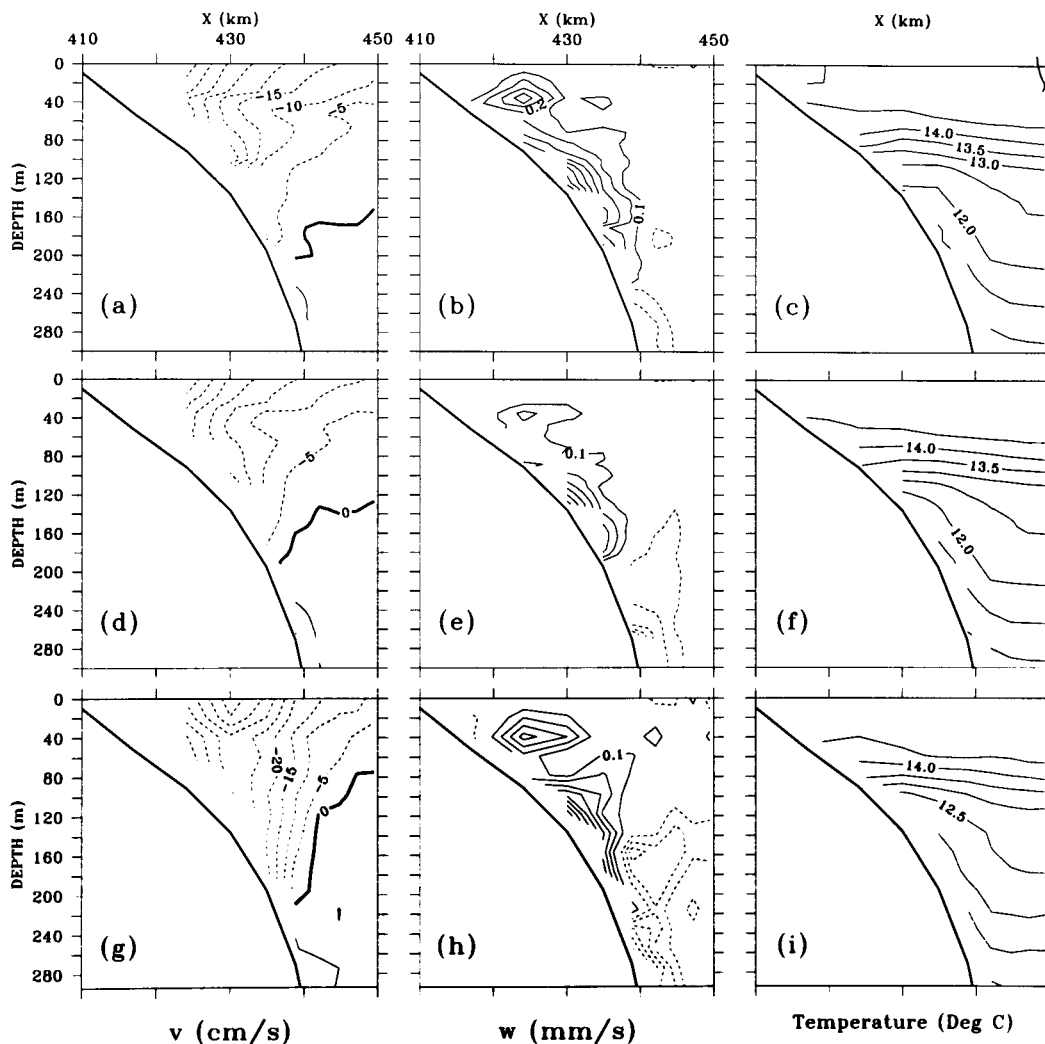
FIG. 6. Cross sections off the Tasmanian shelf ($y = 400$ km) at day 10, as forced by an idealized 8-day period wind stress. (a) Alongshelf velocity v, (b) vertical velocity w, and (c) temperature in the case of $C_D \neq 0$ and maximum wind stress 0.2 Pa. Dashed v contours represent flow in the negative y direction (out of the page). Contour intervals are 5 cm s^{-1}, 0.1 mm s^{-1}, and 0.5°C respectively. (d)–(f) As for (a)–(c) but with $C_D = 0$ and maximum wind stress 0.15 Pa. (g)–(i) As for (a)–(c) but with nonlinear terms $\mathbf{u} \cdot \nabla \mathbf{u}$ switched off.

rather than at day 10 (when the paddle amplitude is a maximum). To understand the circulation shown in Fig. 5b, we first note that the paddle-forced circulation may be broadly regarded as the sum of two components. The first is the incident CTW on the shelf plus the Kelvin wave that propagates to the east on the Victorian coast. The second component of the circulation is the back-scattered Kelvin wave that propagates to the west along the Tasmanian coast together with the scattered CTWs on the western shelf. In terms of the circulation off the northwestern coast of Tasmania, this second component is analogous to that forced by the wind, which drives a westward propagating Kelvin wave along the Tasmanian coast that then generates a scattered CTW field on the shelf. Thus, as shown in Fig. 5, both the paddle and the

wind drive water into the strait between King Island and Tasmania at about the same time. The first component of the paddle circulation adds to this, however, to produce a southward flow on the shelf as well as a flow into the strait north of King Island.

With this idea in mind, consider the paddle forced circulation at day 7 (Figs. 10a,b). As in the wind-forced case (Fig. 8b), the Kelvin wave on the Tasmanian coast drives a flow out of the strait and to the south near the 100-m isobath along the $y = 400$ km section at this time (Fig. 10b). In addition, the presence of the incident CTW drives a northward flow farther offshore. By day 9 the incident CTW circulation on the western shelf is near zero (Figs. 10c,d), and the flow field closely resembles that at day 8 for the wind-forced case. That is,
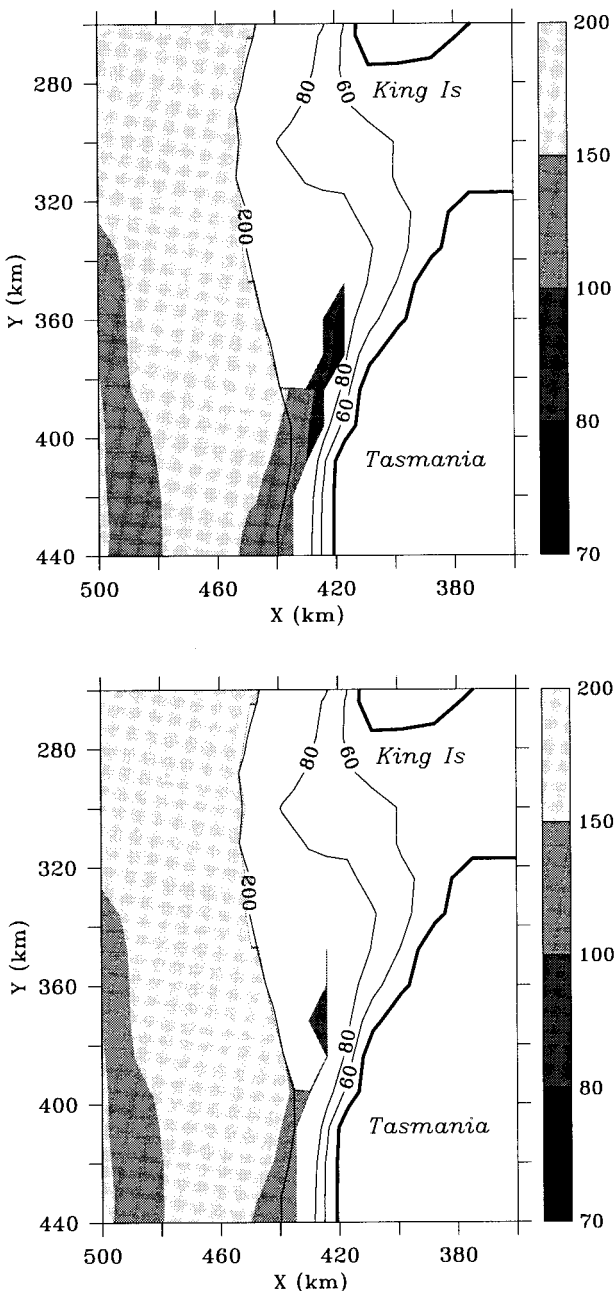
FIG. 7. (a: top) Height of the 12.5°C isotherm, in meters, at day 12 of the idealized wind-forced case. The minimum isotherm depth is 73 m. (b: bottom) As in (a) but with the bottom drag set to zero and the amplitude of the wind stress reduced from 0.2 Pa to 0.15 Pa. The minimum isotherm depth is 84 m. The overlying contours are isobath depths in meters.

a clockwise gyre is found at a depth of 47 m (Figs. 10c and 8d), together with a divergence of velocity at a depth of 100 m (Figs. 10d and 8e).

The upwelling rates associated with this divergence are again large (0.3 mm s⁻¹), but since the subsequent circulation here is to the south (Fig. 5b), water is drawn away from the strait and into deeper water. In contrast

to the wind-forced upwelling, the 12° isotherm is never raised by more than 40 m from its initial depth of 220 m. This is not to say that upwelling driven by CTWs is of no consequence in the real ocean. Data presented in the next section show that the maxima in sea level variations at the paddle region and eastward winds within the strait both occur at about the same time. Since the modeled upwelling velocities for each forcing mechanism are roughly in phase at the $y = 400$ km section, their superposition may enhance upwelling over the shelf slope.

4. Realistic bathymetry and forcing

Here we shall simulate several events in the low-frequency circulation of the western strait region and compare results with current meter and sea level observations. Such a comparison will serve as a further check on the validity of the assumptions made and the boundary conditions adopted. More importantly, it will allow the above results for upwelling to be reappraised under realistic forcing conditions.

An analysis of current meter, sea level, and CTD data obtained during the summer–autumn period of 1991 has shown that the strait waters are generally well mixed and that the currents within the strait are generally barotropic. Variations in the hydrographic structure exist with changes in temperature of 1.5°C and in density of 0.3 kg m⁻³ both across the strait mouth and across the shelf. Profiles of temperature and salinity, obtained off the northwestern shelf of Tasmania during January and May are shown in Fig. 3. Unfortunately, the spatial coverage of CTD data for the shelf region is relatively sparse; four stations spaced 30–40 km apart for each of two cross-shelf CTD sections off Victoria and Tasmania.

Since a more detailed description of the hydrographic structure of the region does not exist, the model was initialized by simply assuming that the summer (or autumn) profiles shown in Fig. 3 pertain to all regions of the model domain. Given the 1°–2°C variations that occur across both the shelf and the strait, however, this idealized specification of the density field will preclude any quantitative comparison of model predictions with point observations of temperature. For simplicity, atmospheric heating/cooling is not considered.

Current meter data from several sites around the strait and shelf were low-pass filtered using the Thompson (1983) filter (with full transmission of signals with periods of 1.7 days and greater), and then resolved along principal axes. At moorings C6 and C10, the major axes are directed into the strait (Fig. 1). Time series of the current (Fig. 11) display significant low-frequency variability in the 10–20-day and 3-day bands. The currents were found to be strongly rectilinear, with minor axis components typically less than 2–3 cm s⁻¹. At the M2 and M3 moorings, the axes are directed along shelf isobaths, with currents that are dominated by variability in the 3-day and 10–20-day bands, respectively.
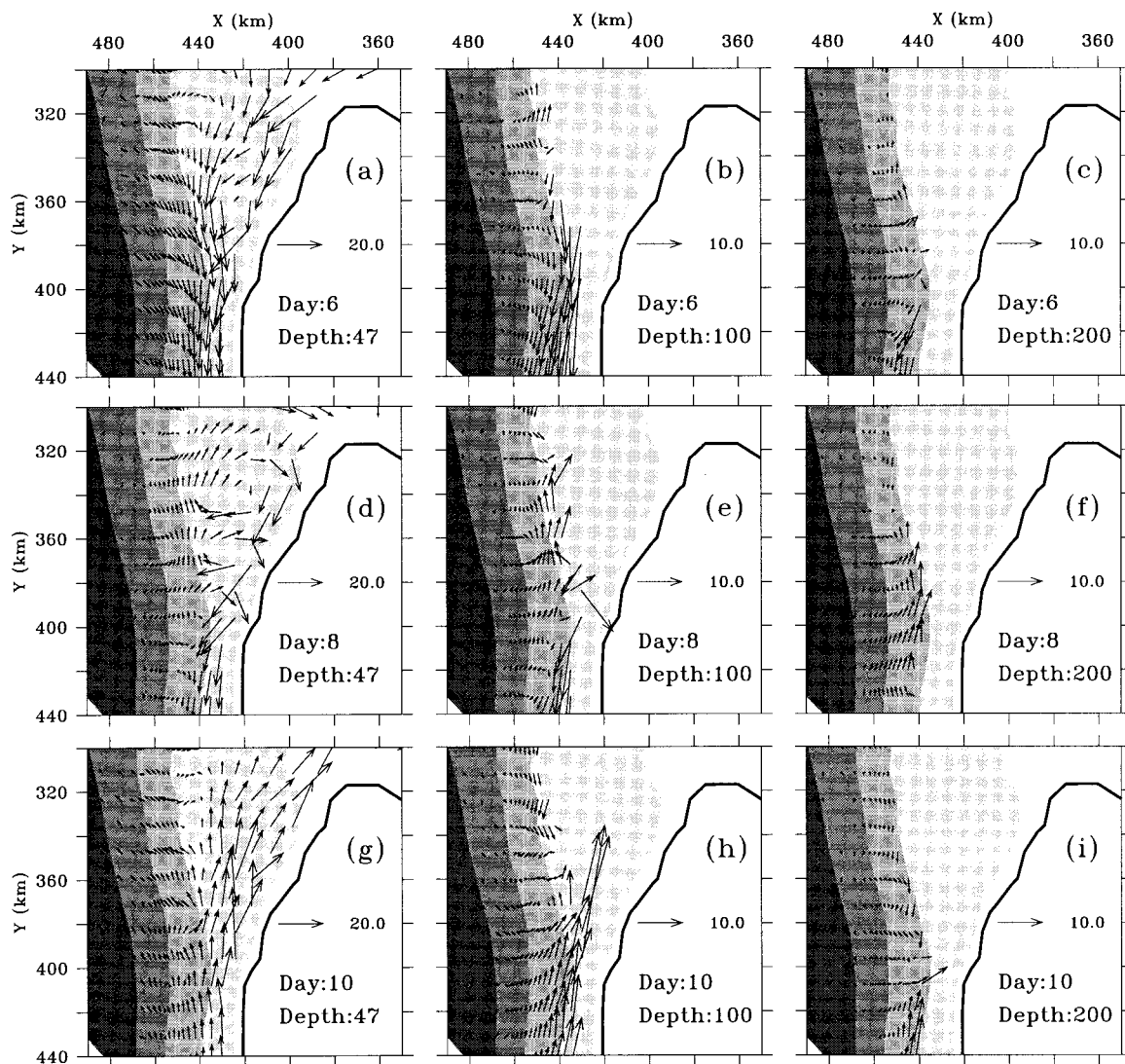
FIG. 8. Current vectors (cm s⁻¹) near the southwest corner of the strait in the idealized wind-forced case, illustrating the divergence-driven upwelling that results from the periodic forcing. Results are presented at depths of 47, 100, and 200 m for days 6 (top row), 8 (center row), and 10 (bottom row). The wind stress is at its westward maximum at day 6, has vanished at day 8, and at its eastward maximum at day 10. Maximum wind stress amplitude is 0.2 Pa. The shaded regions separate isobath contours of 60, 200, 1000, and 2000 m.

Twelve hourly, 1° × 1° surface wind data for the region were obtained from the Australian Bureau of Meteorology, and wind stress calculated using the drag law estimated by Large and Pond (1981). The wind stress was found to be strongly rectilinear with the major axes directed zonally through the strait. As shown in Fig. 11, the winds are characterized by (eastward propagating) storms and the 3–20-day periodicities are evidently coherent with currents within the strait.

Tide gauge data for the region were barometrically adjusted and low-pass filtered (Fig. 12). The resultant time series for Portland and Point Lonsdale on the Victorian coast are evidently coherent with the current

and wind data. To within a day or so, the Portland sea level data and wind data are also in phase. Such a result might be expected since the sea level variability at Portland will be driven by the zonally propagating winds along the South Australian and Victorian shelves. With a phase speed of 10 m s⁻¹ (e.g., Clarke 1977), wind systems take about 6 hours to propagate from Portland to Bass Strait.

a. Summer simulation

From Figs. 11 and 12, it is evident that the largest summertime circulation event occured during January, with changes in wind stress and current speed of
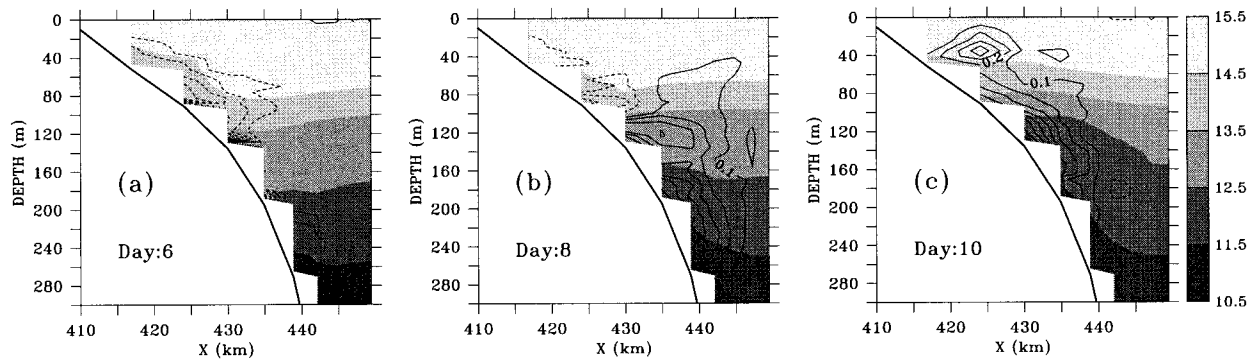
FIG. 9. Sectional views of the vertical velocity at $y = 400$ km for the idealized wind-forced case, at (a) day 6, when the wind stress is 0.2 Pa westward; (b) day 8, when the wind stress is zero; and (c) day 10, when the wind stress is 0.2 Pa eastward. The contour interval is 0.1 mm s^{-1}. The shaded regions separate isotherms as indicated in the key at right.
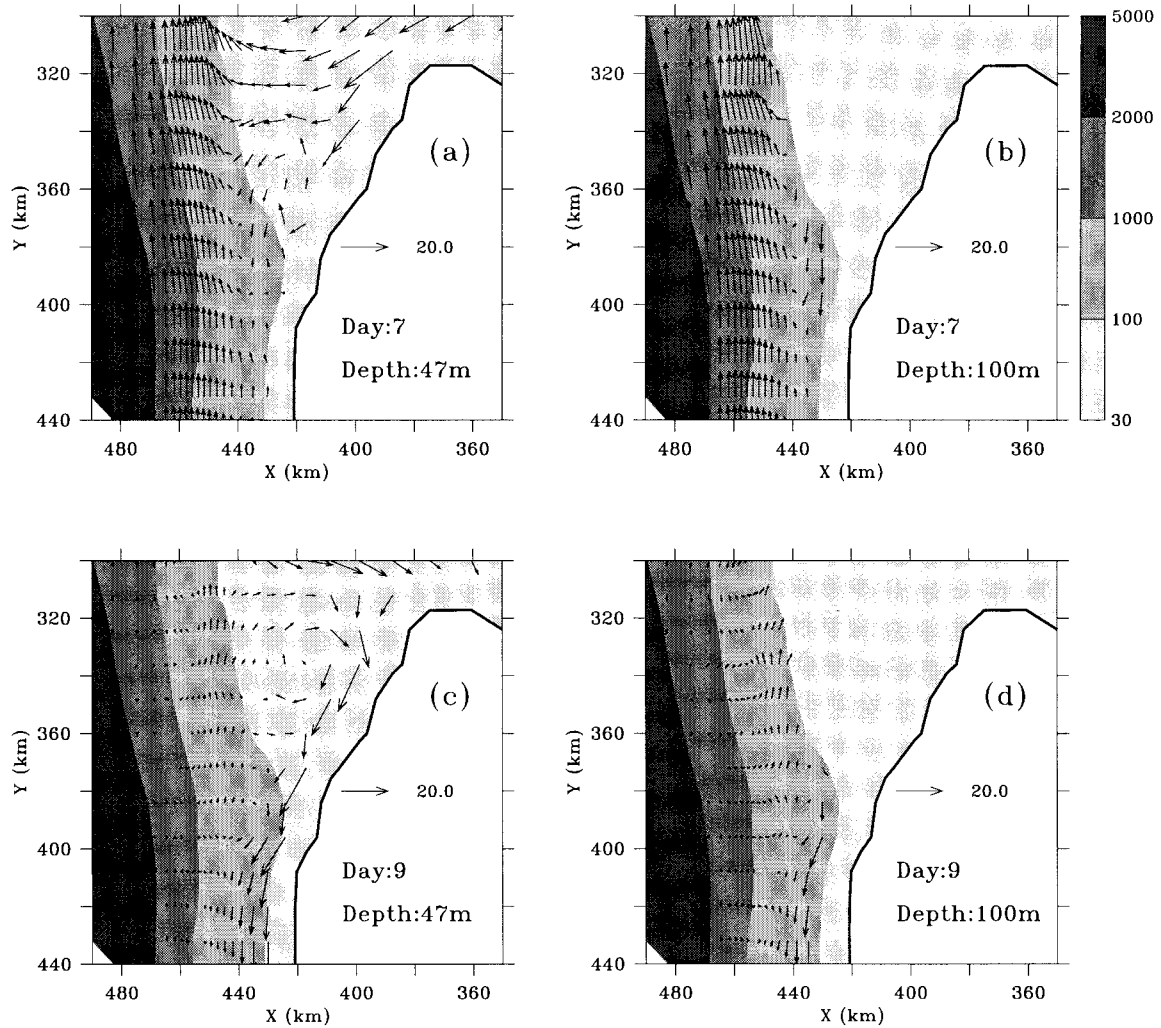
FIG. 10. The circulation driven by the CTW paddle at day 7 (panels a,b) and day 9 (panels c,d). The velocity at day 9 is similar that of the wind-forced case (Figs. 8 e,f), although the subsequent flow for the divergent region is poleward into deeper water (Fig. 5b) and the upwelling is much weaker. The shaded regions separate isobath contours indicated in the right-side key.
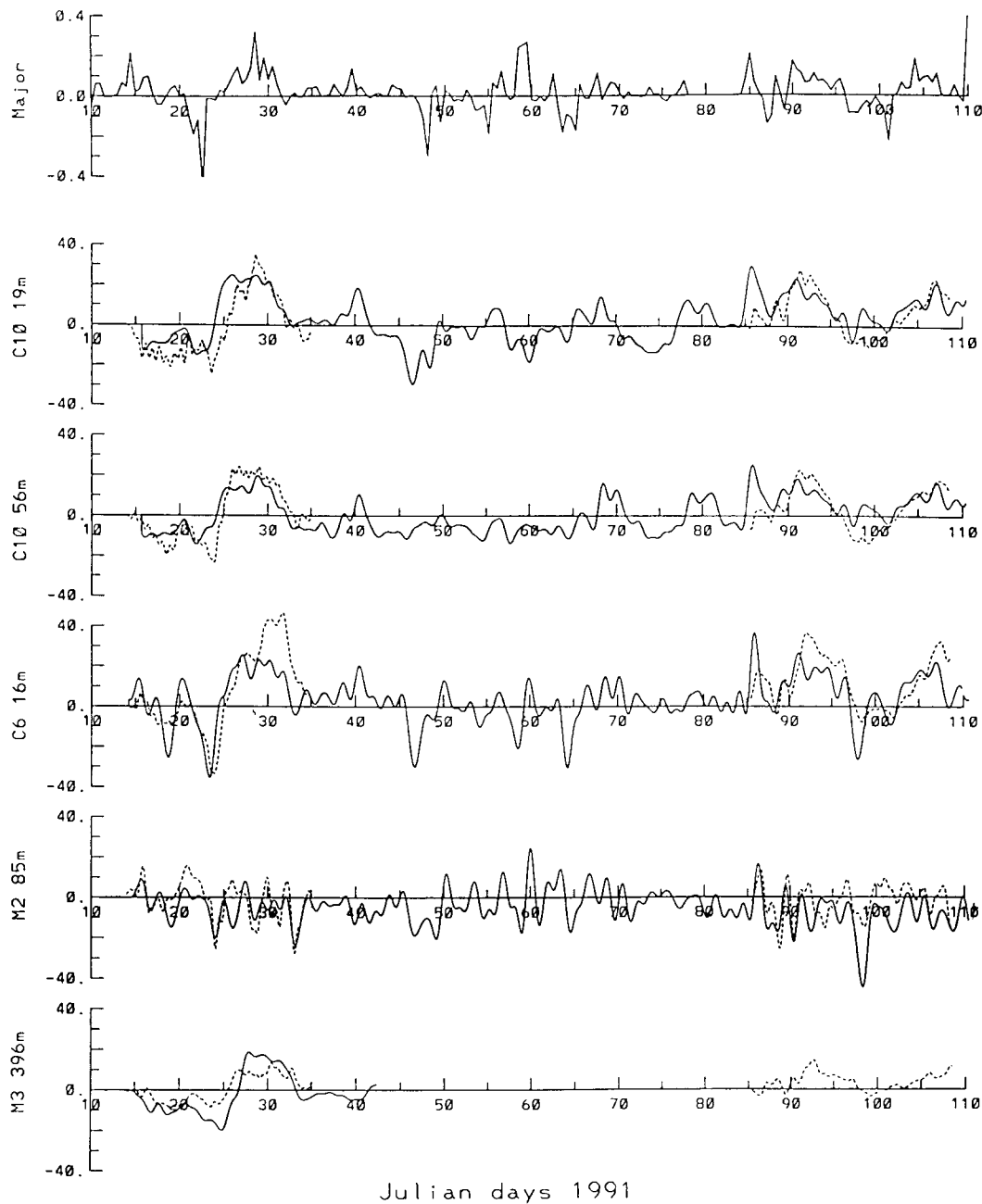
FIG. 11. Top record: the major axis component of wind stress (in Pa) at (39°S, 144°E). Remaining records: the major axis components of observed filtered currents (solid) and simulated currents (dotted) at the sites C10, C6, M2, and M3, (in cm s^{-1}). The instrument depths are indicated. Positive velocities are in the directions of the major axes shown in Fig. 1.

order 0.4Pa and 40 cm s^{-1}. In order to simulate this event, the wind stress was interpolated to the center of each grid cell and the mode 1 CTW paddle was driven using the adjusted Portland sea level record $\eta_P(t)$, whereby $v(x, z, t) = [a_I(t)/\rho_0 f\,]\partial F_1(x, z)/\partial x$ and $a_I = \rho_0 g\eta_P(t)/F_1(0, 0)$. [Note that a mean, calculated over the first 75 days, was subtracted from η_P, and the time series lagged by 1 hour to allow for the trun-

cated length of the model domain along the west Victorian shelf.] The wind stress and sea level time series were then interpolated to each internal time step of the model. To avoid the generation of spurious inertial oscillations, the forcing time series were tapered from zero over the first day using the first quarter-cycle of a 4-day period sine function. Since the model takes a day or two to fully adjust to the forcing, the results
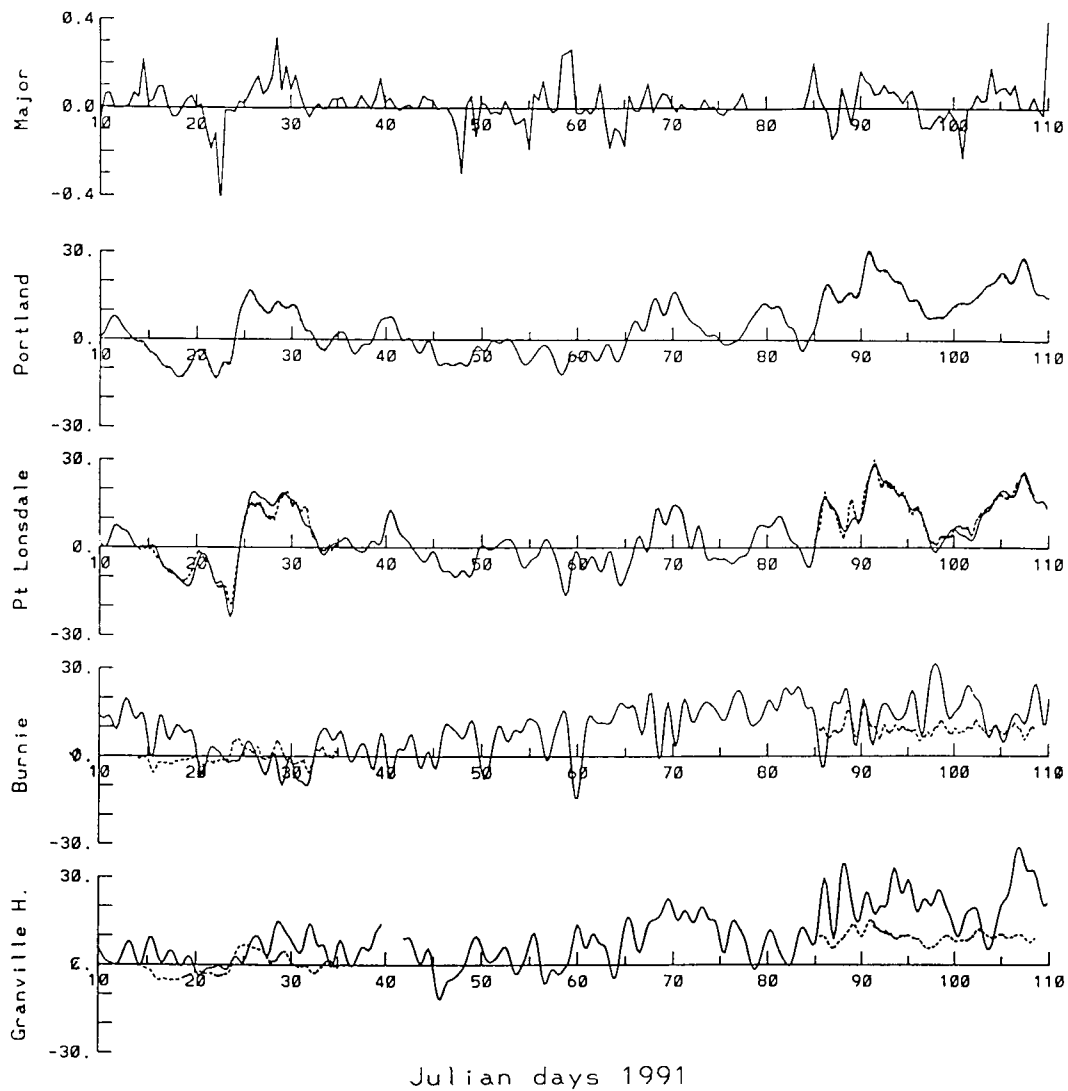
Fig. 12. Top record: the major axis component of wind stress (in Pa) at (39°S, 144°E). Remaining records: the observed filtered and adjusted sea level (solid) and simulated sea level (dotted) at the sites indicated (units cm).

will underpredict the observations over the first 3 days or so. Otherwise, the boundary conditions and tapers used were those outlined in section 3.

The 22-day simulation began at Julian day 13, and an overview of the resultant circulation at the northwest tip of Tasmania at day 31 is shown in Fig. 13. At this time, the winds are directed to the east and sea level at Portland is near a maximum. As found for the idealized circulation forced by the CTW paddle, when currents on the shelf slope are to the south, water is drawn into the strait near King Island and sea level contours bend back into the strait. The signature of the wind-forced component of circulation is also evident nearest the Tasmanian shelf where sea level is negative, leading to an enhancement of the jet directed toward the strait.

Model results for sea level at each of the coastal sites

are presented in Fig. 12. Those for Point Lonsdale are in good agreement with the observations. At this site, the sea level variations are larger than those at Portland due to the additional sea level set up by the zonal winds. At Burnie and Granville Harbour, the model results are in poorer agreement with the observations, although notably, both show that sea level variations are smaller than at Point Lonsdale. The generally smaller *model* response on the Tasmanian coast is expected since sea level variations are fixed to be zero at the southeast corner of the strait by the boundary condition (2.4). The 3-day and 10–20-day variability apparent in the data at these sites is not well reproduced. This variability may be due in part to CTW energy generated on the east Tasmanian coast, which is in turn scattered into the strait. In the model, no such energy source is included.
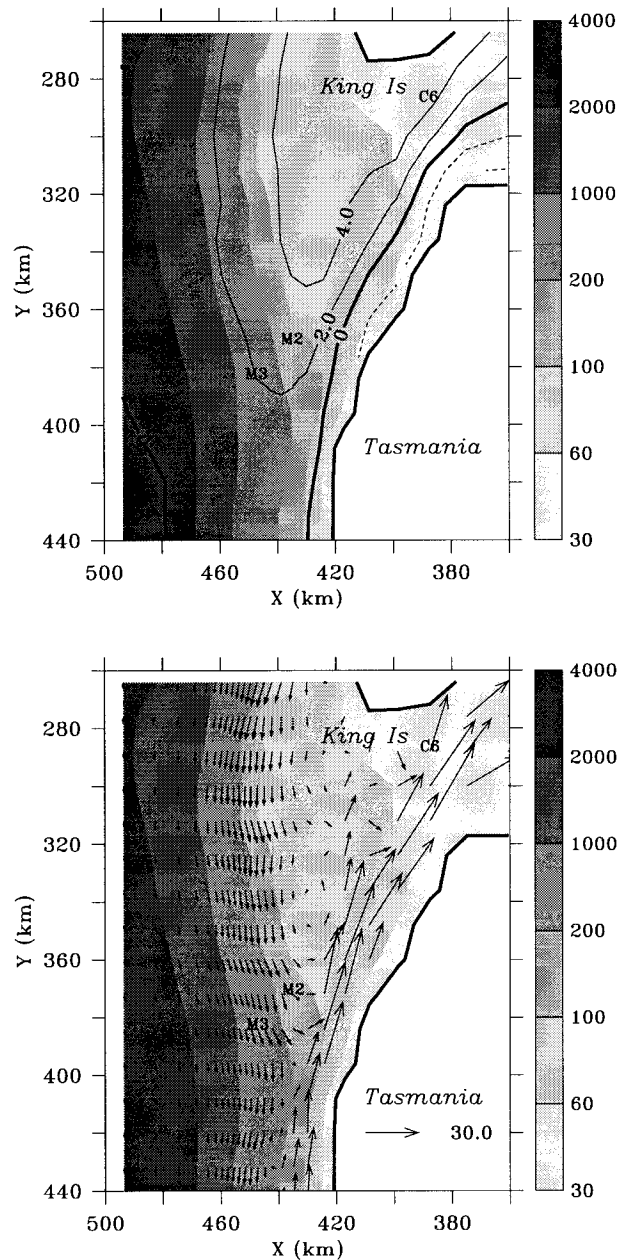
FIG. 13. (top) The sea level field and (bottom) the depth-averaged velocity near Tasmania and King Island for Julian day 31 of the realistic simulation. The units of sea level are cm, and the scale of a 30 cm s⁻¹ velocity vector is shown. The ocean depth (in meters) is shaded.

Note also that the 3-day variability is most apparent in the sea level, current, and wind data obtained closest to the Tasmanian coast. Presumably, the local winds intensify the 3-day band circulation for this region.

Despite these discrepancies, the modeled currents are in reasonable agreement with the observations (Fig. 11). At site C10 (closest to the Victorian coast), the model and observed currents are in good agreement at depths of 19 m and 56 m. The directions of the major axis

components agree to within 15°. [For the model results, the major axis components were computed from the 22 days of simulated current, while for the observations, the axes were computed from all data available.] At site C6 (between King Island and Tasmania), good agreement between the model and observed currents is again found up until day 28, after which the observed currents are smaller than those predicted by the model.

The results for the shelf moorings are shown in Fig. 11. At the M2 site, the model results do simulate some of the 3-day variability apparent in the observations although the agreement is again rather poor. At lower frequencies, the model and observations at the M2 site are in better agreement in that both show relatively little variability in the 10–20-day band. This result should be viewed in the context of the larger 30 cm s⁻¹ (low frequency) currents predicted to exist immediately inshore of the M2 site (Fig. 13b). At the M3 site, the current meter is located well below the thermocline at a depth of 396 m. While the model results at M3 underestimate the magnitude of the observed circulation, they do reproduce the signature of currents associated with the incident mode 1 wave: deep southward (northward) currents that are coherent with currents flowing into (out of) the strait at site C6 (see Fig. 5b).

The forcing by winds and the incident CTW also lead to significant upwelling in deep water. At day 23, when the flow is out of the strait, the flow pattern resembles a linear combination of that shown in Figs. 8a,b and 10a,b just prior to the divergence-driven upwelling. Indeed, at day 25 when the flow reverses direction at the mouth of the strait, horizontal divergence again drives upwelling velocities that exceed 0.4 mm s⁻¹ (36 m day⁻¹). The net effect on the depth of the 11.5° and 12°C isotherms is illustrated in Fig. 14, where the combined effects of upwelling and advection raise 11.5°C water from 160 m to 64 m and drive a plume of cold water 80 km toward the strait. Significant downwelling also occurs: by day 24, the 12° isotherm is depressed by 60 m. Thus, over the 10–15 days of the event modeled, water can be displaced by 100 m in the vertical and by 80 km in the horizontal.

How do these results and conclusions compare with observations of temperature? In Fig. 15, the low-pass filtered temperature records from sites C6 and M2 (solid curves) are plotted along with wind stress. In general agreement with the simulations discussed above, the data at the M2 site show a warming during the downwelling event (days 20–25), and a cooling of a degree or so during the subsequent upwelling event (days 26–30). Classical wind-forced Ekman upwelling is unlikely to be the cause of these temperature changes since, as shown in Fig. 15, the alongshelf component of wind stress is small during these events.

Due to the crude initialization of the model temperature field, the simulated temperature at the M2 site differs by about a degree from the observations. The cooling predicted by the model at other locations is also
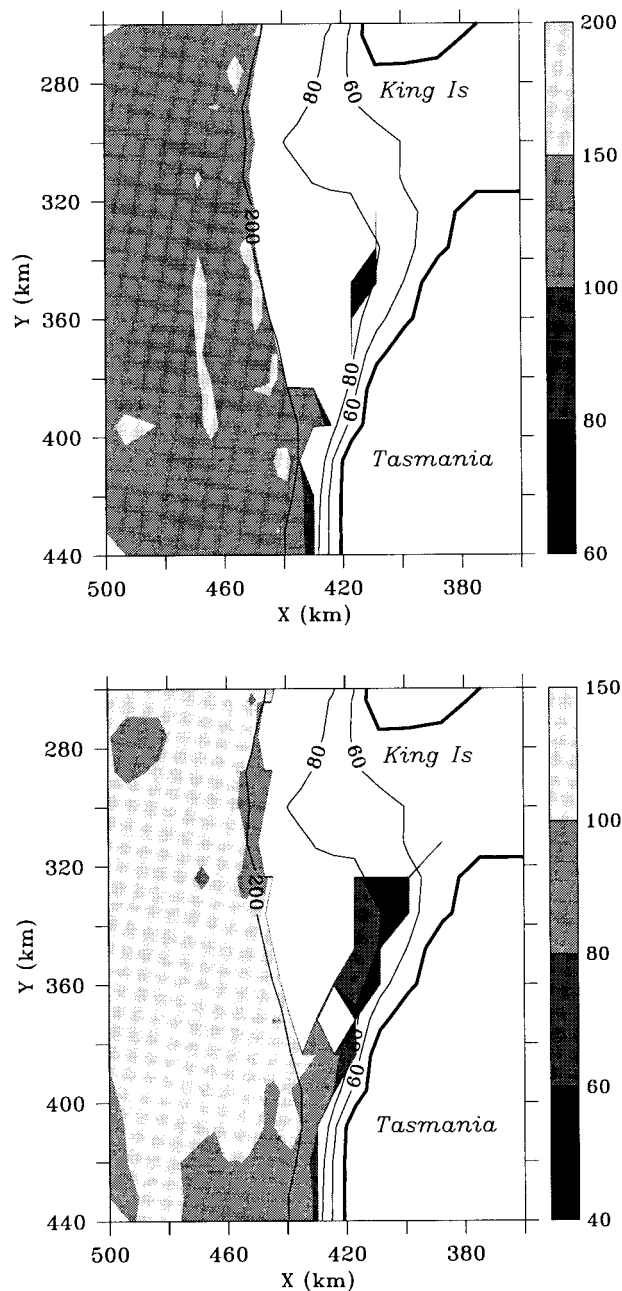
FIG. 14. (a: top) The height of the 11.5°C isotherm, in meters, at Julian day 35 of the realistic summer simulation. The minimum isotherm depth is 64 m. (b: bottom) As in (a) but for the 12°C isotherm. The minimum isotherm depth is 47 m. The overlying contours denote isobath depths in meters.

not found at the M2 site. The difference here is thought to be due to a combination of errors in the initial density field, bathymetry, and location of the model M2 site: the latter lies in a region of considerable velocity shear (Fig. 13) and also near the edge of the upwelling plume (Fig. 14). The model results certainly do show upwelling for the region.

Also shown in Fig. 15 is the temperature record from

site C6, which shows only a 0.5°C cooling at the conclusion of the upwelling event, while the model results suggest that temperature should drop by about a degree. One explanation for this discrepancy is that we have neglected summer heating, which would otherwise act to warm the tidally stirred waters of the strait and so offset the cooling by upwelling.

b. Autumn simulation

The second simulation performed was for 24 days beginning on day 84, the 25th of May. As shown in Fig. 11, this period is characterized by strong wind stress events (0.2 Pa), as well as 20–40 cm s^{-1} variations in currents at the strait mouth. The numerical procedure and forcing was as described above except that CTD data collected in May were used to initialize the model.

The simulated sea level at Point Lonsdale is again in good agreement with the observations (Fig. 12). The modeled sea level variability at both Burnie and Granville Harbour is again small, although the 3-day variability apparent in the observations is larger than for the summer period. The modeled and observed currents at sites C6 and C10 at the strait mouth are also in reasonable agreement. An exception here is the spike in the C6 current at day 97, which has no analog in the wind data and therefore was not reproduced. Results for the M2 site current meter show only crude agreement due to the presence of the 3-day signal.

The solutions are otherwise similar to those found in the summer simulation. In particular, upwelling occurs at day 88 when the westward winds relax, and by day 91 the eastward winds have driven a plume of cool water toward the strait mouth. At day 91, when the eastward wind stress is large, the sea level and velocity field solutions (not presented) are qualitatively similar to those found in the summer simulation (Fig. 13). The upwelling is not as extensive as that found for days 20–35 since the forcing is of smaller amplitude.

Temperature observations at the M2 site (Fig. 15) show a 1°C drop in temperature over days 86–91 when the circulation is upwelling favorable. Similar results are found from the model. However, during days 96–105, the observed temperature increases by 2°C at M2 suggesting that there is considerable downwelling during this period. The data at sites C6 and M2 do show a strong spike of poleward, downwelling-favorable current at around day 97. As noted, such a spike is not evident in the wind data and the downwelling is not reproduced by the model.

5. Summary and discussion

Using a primitive equation model, we have examined the nature of the low-frequency circulation and upwelling for the shelf region west of Bass Strait. An additional goal has been the development and validation of the model and boundary conditions against analytic
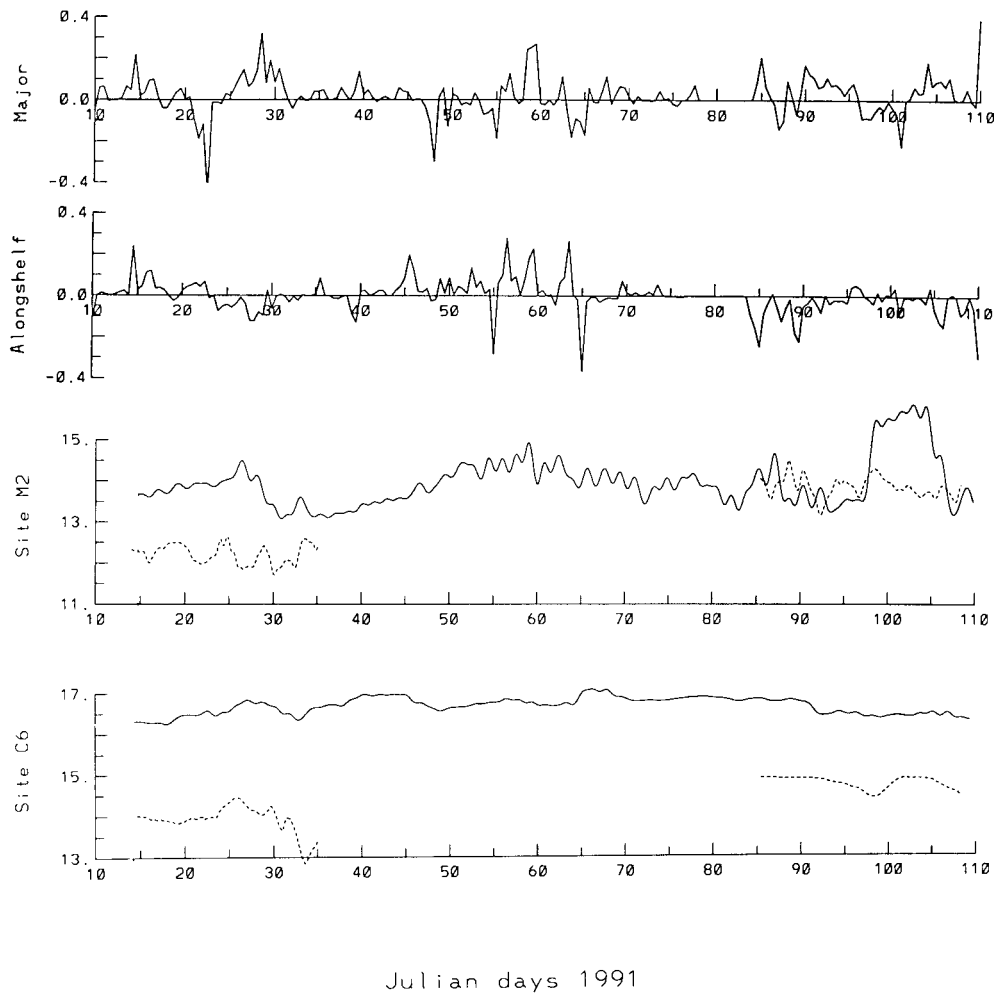
Julian days 1991

FIG. 15. Top two records: The major and alongshelf axis components of wind stress (in Pa) at (39°S, 144°E) where positive values correspond to winds directed eastward into the strait and to the northwest, along the shelf. Bottom two records: The observed temperature (solid) and predicted temperature (dotted) in degrees Celsius from site C6 at a depth of 45 m and from site M2 at a depth of 85 m.

theory and data from the region. To this end, the Princeton Ocean Model was adapted to a rectangular strait geometry, and a new radiation condition was adopted to close the eastern mouth of the strait. The condition (valid at low frequencies) is based on the requirement that pressure perturbations must vanish at the southeast corner of the strait, since CTWs can propagate only with the coast on the left in the Southern Hemisphere. Unlike an Orlanski radiation condition, this boundary condition allows Kelvin wave energy to be backscattered into the strait.

For the rectangular strait geometry, model results forced by an incident CTW and by zonal winds were found to compare well with analytic theories for sea level variability within the strait, indicating that the adopted boundary conditions were performing adequately. The comparisons made were barotropic since the waters of the strait interior are generally well mixed,

and data from the region show the baroclinic component of circulation to be small (e.g., Baines et al. 1991).

The model was then adapted to a semirealistic bathymetry of the Bass Strait region and forced with a periodic zonal wind stress. The results show that the wind-forced motion within the strait acts to drive a 30 cm s^{-1} oscillatory jet off the northwest Tasmanian shelf. The associated cross-isobath flow acts to upwell 12.5°C subthermocline water from depths of 160 m to 80 m and advect it some 60 km toward the strait.

The explanation for this new form of upwelling was that as the periodic (westward) winds relax, the flow over the steep Tasmanian shelf remains poleward and separates from a clockwise gyre that develops over the more gently sloping topography nearer the mouth of the strait. The gyre itself results from the geostrophic adjustment of the flow as the winds relax. The resultant horizontal divergence leads to upwelling rates of 34

m day^{-1}. As the winds intensify to the east, this cold upwelled water is drawn toward the strait. We conclude that the upwelling mechanism is essentially an inviscid linear phenomenon since the deep circulation and upwelling were found to be almost identical to that obtained in the absence of either the bottom drag or the nonlinear terms $\mathbf{u} \cdot \nabla \mathbf{u}$. In shallow water (less than 100 m), bottom drag and nonlinear advection do play a secondary role in enhancing the upwelling of the plume. When water is drawn toward the strait, the bottom boundary layer is upwelling favorable. In addition, the nonlinear terms give rise to a rectified flow of several centimeters per second directed toward the strait.

Some upwelling was also found to result from the scattering of an incident mode 1 CTW since a component of the circulation here resembles that forced by the zonal winds. That is, a Kelvin wave exists that propagates to the west on the Tasmanian shelf and drives a circulation on the western shelf. The additional circulation that is directly associated with the incident CTW, however, subsequently acts to advect upwelled water poleward and into deeper water. Water from depths of 160 m is never upwelled by more than 40 m.

To examine the circulation and upwelling under realistic conditions, two simulations were made by forcing the model with regional winds and by a mode 1 CTW paddle, modulated using low-pass filtered sea level data from Portland. The results were found to be in good agreement with current and sea level variability in the 10–20-day band observed nearest the Victorian coast. Sea level observations on the Tasmanian coast were not well predicted, although during summer both model and observations show that the variability is much reduced over that found at Point Lonsdale. On the shelf, the weak 10–20-day variablity at the M2 site was predicted, while at the deep M3 site the signature of the circulation associated with forcing by the paddle was reproduced: southward (northward) currents coherent with the 10–20-day band currents flowing into (out of) the strait. A notable discrepancy was the poor prediction of the 3-day band variability observed nearest the Tasmanian shelf. Possibly, part of this signal is generated on the east Tasmanian shelf and is scattered into the strait. In the model, no such energy source was included, sea level being fixed to zero at the southeastern corner of the strait.

Perhaps the most important result obtained is the prediction that the circulation on the western shelf may upwell subthermocline water into the strait mouth. The evidence to support this prediction is indirect being based upon (i) the partial agreement between the modeled and observed currents and sea level in the 10–20-day band of variability, and (ii) the temperature data from the M2 shelf site. Admittedly, the model results are in poor agreement with the M2 temperature data, although the discrepancy here is possibly due to errors in bathymetry, positions of the model sites, and the initial density field. The model certainly does predict

upwelling in the region of the M2 site, and other observations obtained near King Island do show episodic reductions in bottom temperature during intense storms (Blackman et al. 1987). Also, maxima in chlorophyll-a are observed in the region (Gibbs et al. 1986).

In conclusion, the strait boundary condition developed should prove useful for modeling studies of other straits, and the new form of episodic upwelling outlined may be important for other sea–strait regions. Necessary conditions for such upwelling are that intense periodic winds exist in the strait region and that the shelf adjacent to the strait should narrow in the direction of CTW propagation. Unlike Ekman upwelling, the upwelling described here is essentially a subsurface phenomena. Little or no signature may be present in surface temperature, and such upwelling may exist in other regions but remain undetected.

REFERENCES

Baines, P. G., G. Hubbert, and S. B. Power, 1991: Fluid transport through Bass Strait. *Contin. Shelf Res.,* **11,** 269–293.

Black, K. P., 1992: Evidence of the importance of deposition and winnowing of surficial sediments at a continental shelf scale. *J. Coastal Res.,* **8,** 319–331.

Blackman, D. R., J. B. Hinwood, and G. T. Lieonart, 1987: Temperature anomaly in western Bass Strait. *Aust. J. Mar. Freshwater Res.,* **38,** 191–195.

Blumberg, A. F., and G. L. Mellor, 1987: A description of a three-dimensional coastal ocean circulation model. *Three-Dimensional Coastal Ocean Models,* N. Heaps, Ed., Amer. Geophys. Union, 208 pp.

Brink, K. H., and D. C. Chapman, 1985: Programs for computing properties of coastal-trapped waves and wind-driven motions over the continental shelf and slope. Tech. Rep. WHOI-85-17, 99 pp. [Available from Woods Hole Oceanogr. Inst., Woods Hole, MA 02543.]

Cahill, M. L., J. H. Middleton, and B. R. Stanton, 1991: Coastal-trapped waves on the west coast of South Island, New Zealand. *J. Phys. Oceanogr.,* **21,** 541–557.

Chapman, D. C., 1985: Numerical treatment of cross-shelf open boundaries in a barotropic coastal ocean model. *J. Phys. Oceanogr.,* **15,** 1060–1075.

Church, J. A., and H. J. Freeland, 1987: The energy source for the coastal-trapped waves in the Australian Coastal Experiment region. *J. Phys. Oceanogr.,* **17,** 289–300.

Clarke, A. J., 1977: Observations and numerical evidence for wind-forced coastal-trapped long waves. *J. Phys. Oceanogr.,* **7,** 231–247.

Davies, A. M., and J. E. Jones, 1992: A three dimensional circulation

model of the Celtic and Irish Seas. *Contin. Shelf Res.,* **12,** 159–188.

Fandry, C. B., G. D. Hubbert, and P. C. McIntosh, 1985: Comparison of predictions of a numerical model and observations of tides in Bass Strait. *Aust. J. Mar. Freshwater Res.,* **36,** 737–752.

Freeland, H. J., F. M. Boland, J. A. Church, A. J. Clarke, A. M. G. Forbes, A. Huyer, R. L. Smith, R. O. R. Y. Thompson, and N. J. White, 1986: The Australian Coastal Experiment: A search for coastal-trapped waves. *J. Phys. Oceanogr.,* **16,** 1230–1249.

Gardiner-Garden, R. S., and J. F. Middleton, 1996: Coastal-trapped wave scattering by a strait: Model verification. Dept. Applied Math. Rep. AM96/22, 29 pp. [Available from School of Mathematics, University of New South Wales, Sydney 2052, New South Wales, Australia.]

Gibbs, C. F., M. Tomczak Jr., and A. R. Longmore, 1986: The nutrient regime of Bass Strait. *Aust. J. Mar. Freshwater Res.,* **37,** 451–466.

Gill, A. E., 1982: *Atmosphere–Ocean Dynamics.* Academic Press, 662 pp.

Hannah, C. G., 1992: Geostrophic control with wind forcing: Application to Bass Strait. *J. Phys. Oceanogr.,* **22,** 1596–1599.

Large, W. G., and S. Pond, 1981: Open ocean momentum flux measurements in moderate to strong winds. *J. Phys. Oceanogr.,* **11,** 324–336.

McCreary, J. P., Y. Fukamachi, and P. K. Kundu, 1991: A numerical investigation of jets and eddies near an eastern ocean boundary. *J. Geophys. Res.,* **96,** 2515–2534.

Mellor, G. L., T. Ezer, and L.-Y. Oey, 1994: On the pressure gradient conundrum of sigma coordinate ocean models. *J. Atmos. Oceanic Technol.,* **11,** 1126–1134.

Middleton, J. F., 1991: Coastal-trapped wave scattering into and out of straits and bays. *J. Phys. Oceanogr.,* **21,** 681–694.

——, 1994: The baroclinic response of straits and bays to coastal-trapped wave scattering. *J. Phys. Oceanogr.,* **24,** 521–539.

——, and F. Viera, 1991: The forcing of low frequency motions within Bass Strait. *J. Phys. Oceanogr.,* **21,** 695–708.

——, and K. P. Black, 1994: The low frequency circulation in and around Bass Strait: A numerical study. *Contin. Shelf Res.,* **14,** 1495–1521.

Oey, L.-Y., J. Manning, H. T. Jo, and K. W. You, 1995: A plume and wind-driven circulation model of the New York Bight. *Quantitative Skill Assessment for Coastal Ocean Models,* D. R. Lynch and A. M. Davies, Eds., Coastal and Estuarine Studies, Vol. 41, Amer. Geophys. Union, 329–348.

Roed, L. P., B. Hackett, B. Gjevik, and L. I. Eide, 1995: A review of the Metocean Modeling Project (MOMOP). Part 1: Model comparison study. *Quantitaive Skill Assessment for Coastal Ocean Models,* D. R. Lynch and A. M. Davies, Eds., Coastal and Estuarine Studies, Vol. 41, Amer. Geophys. Union, 285–306.

Slordal L. H., E. A. Martinsen, and A. F. Blumberg, 1994: Modeling the response of an idealized coastal ocean to a traveling storm and to flow over bottom topography. *J. Phys. Oceanogr.,* **24,** 1689–1705.

Thompson, R. O. R. Y., 1983: Low-pass filters to suppress inertial and tidal frequencies. *J. Phys. Oceanogr.,* **13,** 1077–1083.

Webster, I., and S. Narayanan, 1988: Low frequency current variability on the Labrador shelf. *J. Geophys. Res.,* **93,** 8163–8173.

Werner, F. E., J. O. Blanton, D. R. Lynch, and D. K. Savidge, 1993: A numerical study of continental shelf circulation of the U.S. South Atlantic Bight during autumn of 1987. *Contin. Shelf Res.,* **13,** 971–997.

Wilkin, J., and D. C. Chapman, 1990: Scattering of coastal-trapped waves by irregularities in coastline and topography. *J. Phys. Oceanogr.,* **20,** 396–421.

Wright, D. G., and K. R. Thompson, 1983: Time-averaged forms of the nonlinear stress law. *J. Phys. Oceanogr.,* **13,** 341–345.

——, D. A. Greenberg, and F. G. Majaess, 1987: The influence of bays on adjusted sea level over adjacent shelves with application to the Labrador shelf. *J. Geophys. Res.,* **92,** 14 610–14 620.